Controlling the growth of $Cs_3Sb_2I_{9-x}Cl_x$ thin films by adjusting annealing time in ambient air

FEI ZHAO[1,*], YIXIN GUO[2,*]
[1]*School of Photoelectric Engineering, Changzhou Institute of Technology, Changzhou, Jiangsu, 213032, China*
[2]*Department of Physics, Shanghai Normal University, Shanghai 200233, China*

The development of all-inorganic antimony (Sb)-based perovskite-inspired solar cells (PISCs) has garnered significant interest owing to their superior stability and non-toxic nature. Nevertheless, the fabrication of high-quality all-inorganic Sb-based perovskite-inspired thin films remains a significant obstacle. Herein, all-inorganic $Cs_3Sb_2I_{9-x}Cl_x$ thin films were synthesized by adjusting the annealing time in ambient air. As the annealing time increases from 6 to 10 min, the number of holes in $Cs_3Sb_2I_{9-x}Cl_x$ thin film reduces. Simultaneously, its defect density decreases. However, with a further extension of the annealing time to 14 min, the number of holes for $Cs_3Sb_2I_{9-x}Cl_x$ thin film increases and its defect density improves. Consequently, the $Cs_3Sb_2I_{9-x}Cl_x$ thin film with annealing 10 min exhibits the best growth quality.

(Received October 11, 2025; accepted February 2, 2026)

Keywords: $Cs_3Sb_2I_{9-x}Cl_x$ thin films, Annealing time, Hole, Defect

1. Introduction

Despite the groundbreaking efficiency milestones achieved in organic-inorganic lead halide perovskite solar cells (PSCs), exemplified by a photoelectric conversion efficiency (PCE) of 27% [1], their path toward mass commercialization is fundamentally challenged by the intrinsic toxicity of lead (Pb) and the thermal instability associated with organic constituents. We have fabricated all-inorganic Pb-based perovskite thin films via a solution-processing method and have applied them in solar cells [2-4]. High thermal stability for Pb-based perovskites is achieved, indicating that the thermal instability issue of perovskite solar cells has been effectively addressed [5-8]. However, the inherent toxicity of Pb remains unresolved [9]. Therefore, it is crucial to develop non-toxic and environmentally friendly perovskite thin films.

Owing to the analogous properties of tin (Sn) and Pb, Sn-based perovskites have emerged as prominent candidates for efficient PSCs without Pb [10]. However, the fast oxidation of Sn^{2+} to Sn^{4+} for Sn-based perovskites under ambient atmosphere critically undermines its stability. Given this challenge, Sb-based perovskite-inspired materials have garnered significant interest as a promising inorganic Pb-free absorbers [11-13]. Currently, the fabrication of Sb-based perovskite-inspired thin films is primarily accomplished by the solution spin-coating method [14,15]. The solution-based spin-coating technique has played a pivotal role as a well-established and relatively straightforward protocol for the synthesis of high-quality Sb-based perovskite thin films [16]. To the best of our knowledge, the fabrication of Sb-based perovskite-inspired thin films necessitates the use of a glovebox, thereby complicating the process. Moreover, the successful preparation of the Sb-based thin films in ambient air has not been reported so far.

In this work, high-quality $Cs_3Sb_2I_{9-x}Cl_x$ thin films were fabricated by precisely controlling the annealing time in ambient air. A systematic investigation into the microstructural evolution of the films during annealing has been conducted to elucidate the underlying mechanisms. It was determined that varying the annealing duration directly influences the crystallization pathway by promoting nucleation, thereby effectively manipulating the number of surface holes and defect density. Consequently, this method enables the attainment of $Cs_3Sb_2I_{9-x}Cl_x$ thin films with compact morphology and reduced defect densities.

2. Experimental

2.1. Preparation of $Cs_3Sb_2I_{9-x}Cl_x$ thin films

The entire fabrication process of $Cs_3Sb_2I_{9-x}Cl_x$ thin film was conducted under ambient atmospheric condition. A precursor solution was subsequently formulated by dissolving CsI (0.75 M, 99.9%), SbI_3 (0.25 M, 98%), and $SbCl_3$ (0.3125 M, 99.95%) in dimethylformamide (DMF, 99.8%), which was then stirred at 70 °C for 3 h. This solution was spin-coated onto the ITO substrates at 3000 rpm for 30 s. To control crystallization, 65 μL of anisole was introduced as an anti-solvent at 8 s after initiating the spin-coating process. Finally, the as-deposited thin films

were subjected to SbI_3 vapor annealing at 240 °C for varied time (6, 10, and 14 min).

2.2. Characterizations

The crystal structure of the $Cs_3Sb_2I_{9-x}Cl_x$ sample was characterized by X-ray diffraction (XRD). The surface morphology of the $Cs_3Sb_2I_{9-x}Cl_x$ sample was analyzed using field emission scanning electron microscopy (FE-SEM). The elemental composition of the $Cs_3Sb_2I_{9-x}Cl_x$ film was characterized by X-ray photoelectron spectroscopy (XPS) technology. The Raman spectra of the $Cs_3Sb_2I_{9-x}Cl_x$ samples were recorded on a LabRAM instrument using 532 nm laser excitation.

3. Results and discussions

3.1. XRD analysis

Fig. 1a shows the XRD patterns of $Cs_3Sb_2I_{9-x}Cl_x$ samples subjected to different annealing times. As observed in Fig. 1a, three distinct diffraction peaks are present at 25.86°, 30.08°, and 35.22°. The peak at 25.86° corresponds to the (201) crystal plane of $Cs_3Sb_2I_{9-x}Cl_x$ sample [10]. The peaks at 30.08° and 35.22° are attributed to the crystal planes of the ITO substrate [17]. Notably, the intensity of the (201) diffraction peak varies significantly among $Cs_3Sb_2I_{9-x}Cl_x$ samples with different annealing times, which can be attributed to the influence of annealing time. It is worth noting that the intensity of the ITO diffraction peak at 30.08° also exhibits considerable variation in different $Cs_3Sb_2I_{9-x}Cl_x$ sample. This is due to the overlap between the diffraction peak of the ITO substrate and the diffraction peak of the crystal plane for $Cs_3Sb_2I_{9-x}Cl_x$ sample at this position. The superposition of these peaks results in distinctly different diffraction intensities. Fig. 1b illustrates the intensity values of the (201) diffraction peak for $Cs_3Sb_2I_{9-x}Cl_x$ samples under different annealing times. As shown in Fig. 1b, when the annealing time increases from 6 min to 10 min, the intensity of the (201) diffraction peak increases. This indicates enhanced crystallinity of $Cs_3Sb_2I_{9-x}Cl_x$ sample. However, the intensity of the (201) peak decreases as the annealing time further increases to 14 min, suggesting a reduction in crystallinity. Therefore, the optimal crystallinity of $Cs_3Sb_2I_{9-x}Cl_x$ sample is achieved at an annealing time of 10 min.

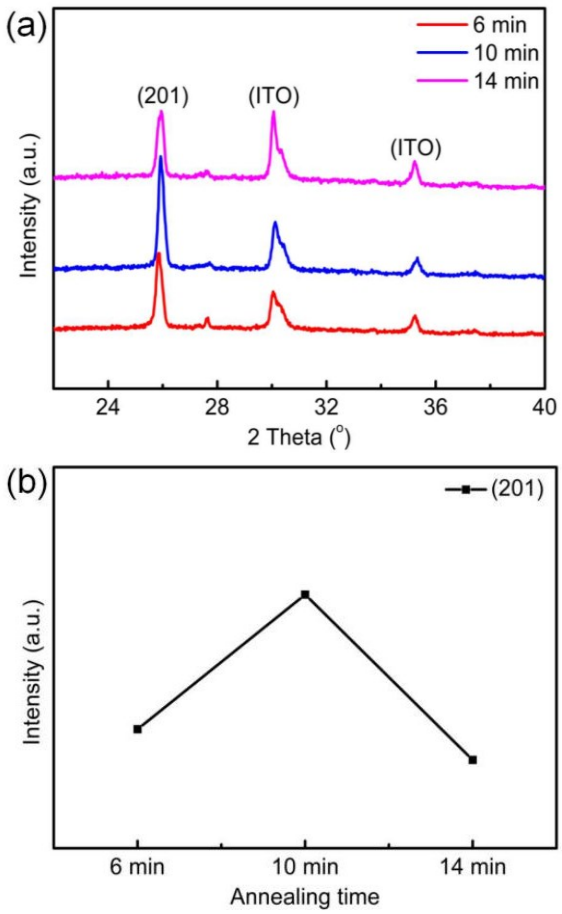

Fig. 1. (a) XRD patterns of $Cs_3Sb_2I_{9-x}Cl_x$ samples with different annealing times. (b) Intensity values of (201) peak for $Cs_3Sb_2I_{9-x}Cl_x$ samples with various annealing times (colour online)

3.2. SEM analysis

The surface morphology of $Cs_3Sb_2I_{9-x}Cl_x$ sample was examined using SEM (Figs. 2a-2c). As observed in Fig. 2a, $Cs_3Sb_2I_{9-x}Cl_x$ sample annealed for 6 min displays many holes, suggesting low crystallinity and a considerable number of defects. With an increase in annealing time to 10 min, $Cs_3Sb_2I_{9-x}Cl_x$ sample becomes more compact, indicating enhanced crystallinity and a reduction in defects [18-20]. Prolonging the annealing time to 14 min, however, results in the reemergence of a large number of holes, signifying a decline in crystal quality and an increase in defect density. Consequently, the sample annealed for 10 min exhibits the best crystallinity and the fewest defects. This phenomenon can be explained by the fact that short-term annealing (6 min) leads to incomplete grain growth, resulting in the formation of pores and the introduction of defects. When the annealing time is increased from 6 min to 10 min, $Cs_3Sb_2I_{9-x}Cl_x$ sample obtains sufficient crystallization time and forms a denser morphology, which significantly reduces the number of holes and defects. Over-annealing (14 min), however, may lead to decreased crystallinity and increased defect count for $Cs_3Sb_2I_{9-x}Cl_x$ sample. Hence, the precise control of annealing time is crucial for optimizing the structural properties of $Cs_3Sb_2I_{9-x}Cl_x$ sample.

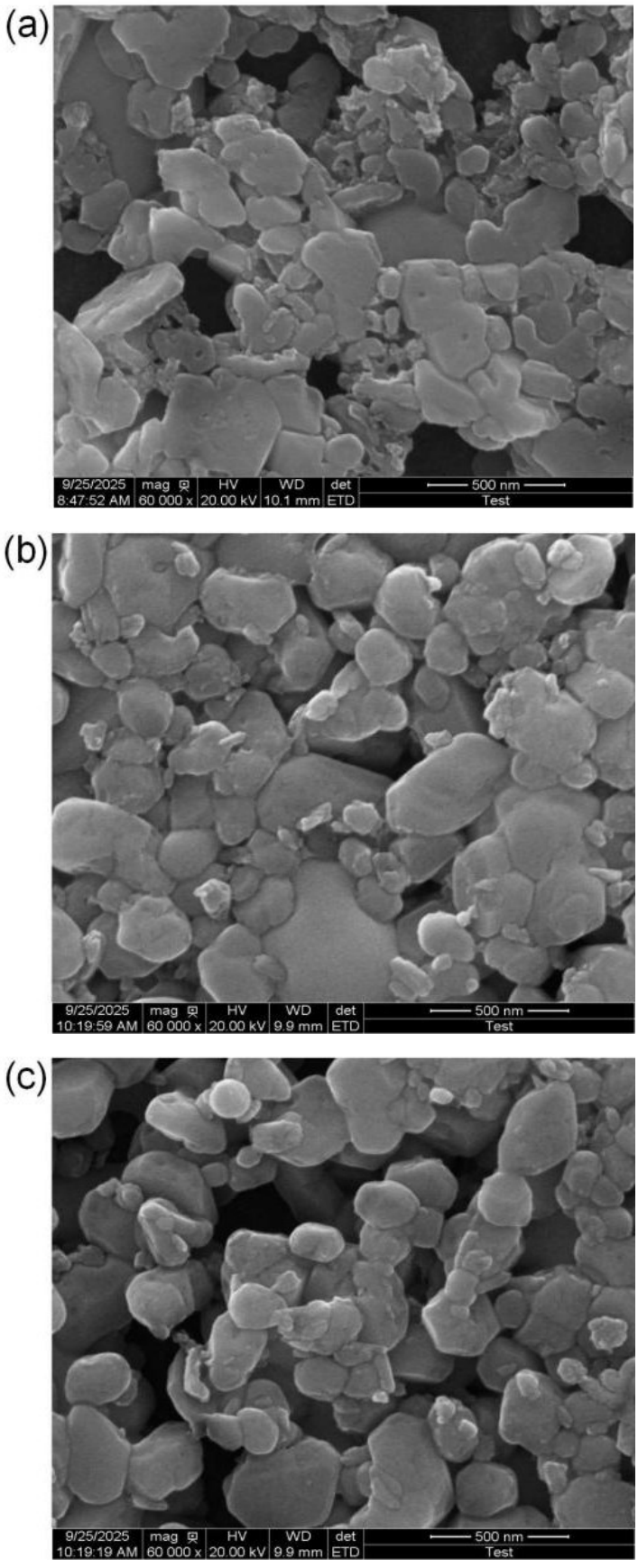

Fig. 2. Surface SEM morphology of $Cs_3Sb_2I_{9-x}Cl_x$ samples with annealing times of (a) 6 min, (b) 10 min and (c) 14 min

3.3. XPS analysis

XPS test was performed to determine the elemental valence states in $Cs_3Sb_2I_{9-x}Cl_x$ samples. Fig. 3 displays the core-level XPS spectra of Cs 3d, Sb 3d, I 3d, and Cl 2p for $Cs_3Sb_2I_{9-x}Cl_x$ sample annealed at 10 min. The spin-orbit splitting of the Cs 3d core level yields doublet peaks at 724.36 eV ($3d_{5/2}$) and 738.32 eV ($3d_{3/2}$), corresponding to the Cs^+ charge state. Similarly, the Sb 3d core level exhibits a doublet with binding energies of 530.63 eV ($3d_{5/2}$) and 540.02 eV ($3d_{3/2}$), corresponding to the Sb^{3+} charge state. The I 3d core level presents two peaks at 618.86 eV ($3d_{5/2}$) and 630.37 eV ($3d_{3/2}$), corresponding to the I^- charge state. For Cl 2p, the peaks located at 198.56 eV ($2p_{3/2}$) and 200.96 eV ($2p_{1/2}$) are assigned to Cl^-. The observed valence states of Cs^+, Sb^{3+}, I^-, and Cl^- confirm the phase purity of the $Cs_3Sb_2I_{9-x}Cl_x$ sample.

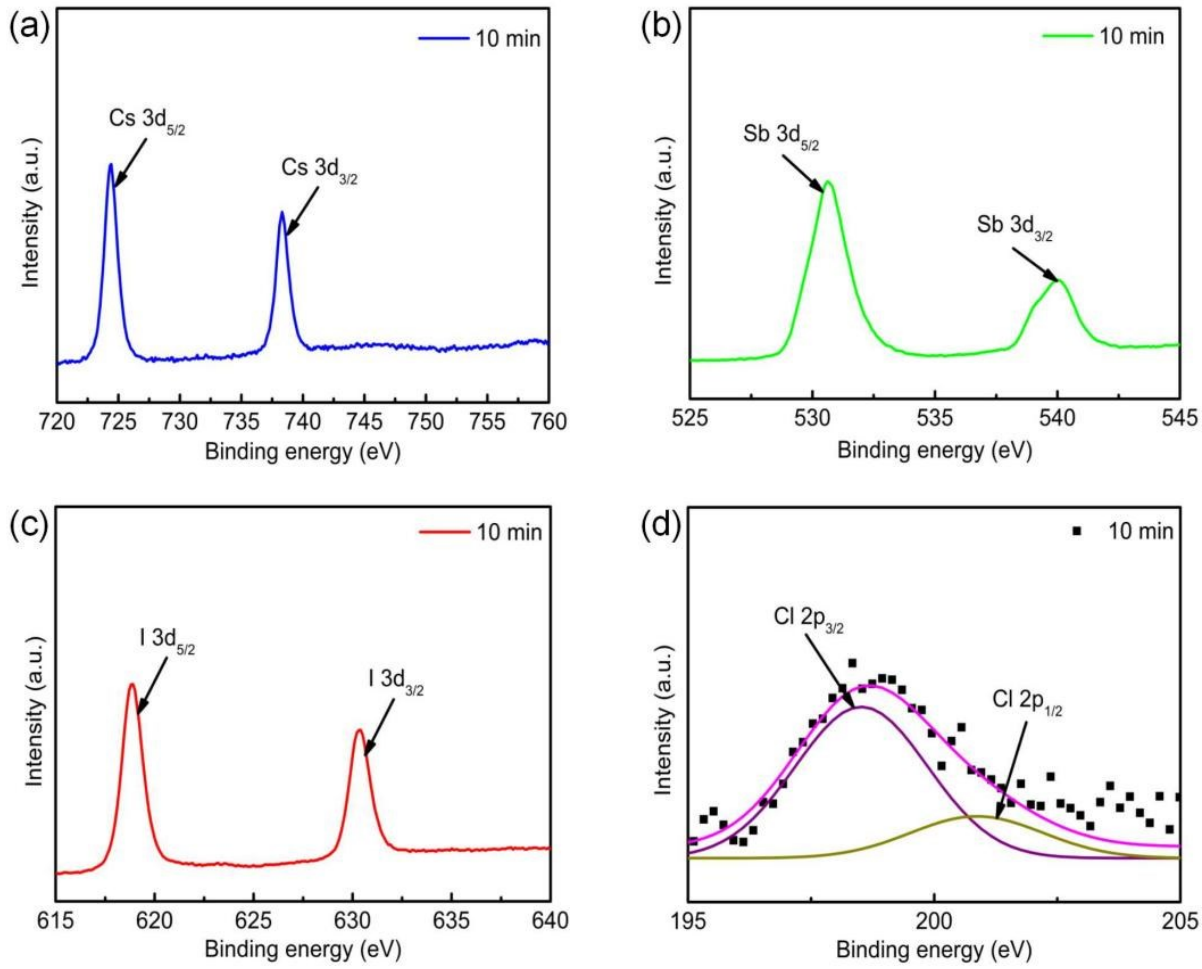

Fig. 3. XPS spectra of (a) Cs 3d core level, (b) Sb 3d core level, (c) I 3d core level and (d) Cl 2p core level for $Cs_3Sb_2I_{9-x}Cl_x$ thin film annealed at 10 min (colour online)

3.4. Raman analysis

Fig. 4 shows the Raman spectra of $Cs_3Sb_2I_{9-x}Cl_x$ samples with different annealing times. From Fig. 4, it can be seen that in all $Cs_3Sb_2I_{9-x}Cl_x$ samples, a distinct broad stretching mode at ~150 cm^{-1} is attributed to the persistence of $Cs_3Sb_2I_{9-x}Cl_x$ phase [21,22]. When the annealing time increases from 6 min to 14 min, $Cs_3Sb_2I_{9-x}Cl_x$ sample undergos displacement. This is due to the influence of annealing time. In addition, when the annealing time increases from 6 min to 10 min, the characteristic peak intensity of $Cs_3Sb_2I_{9-x}Cl_x$ sample increases, indicating that its phase structure is more stable. However, as the annealing time increases to 14 min, the characteristic peak intensity of $Cs_3Sb_2I_{9-x}Cl_x$ sample weakens, indicating that its phase structure is unstable. Therefore, when the annealing time is 10 min, the performance of $Cs_3Sb_2I_{9-x}Cl_x$ sample is optimal.

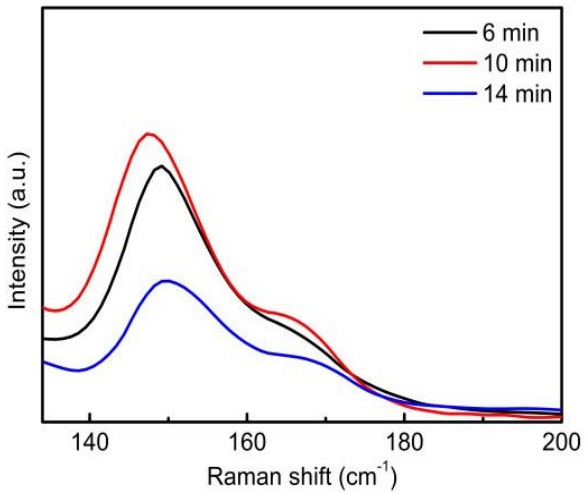

Fig. 4. Raman spectra of $Cs_3Sb_2I_{9-x}Cl_x$ thin films with different annealing times (colour online)

4. Conclusions

High-quality all-inorganic $Cs_3Sb_2I_{9-x}Cl_x$ thin films were fabricated via varying annealing time. It was observed that extending the annealing time from 6 to 10 min may result in reduced holes and a concomitant reduction in the defect density. Further prolonging the annealing to 14 min, however, may lead to a enhancement in the number of holes and the improvement of the defect density. Thus, the $Cs_3Sb_2I_{9-x}Cl_x$ thin film with the optimal annealing time of 10 min owns the minimum number of holes and the lowest defect density.

Acknowledgements

This work was financially supported by the Changzhou Scientific and Technological Program grant (Grant No. CJ20250087) and the National Natural Science Foundation of China (Grant No. 12304043).

References

[1] Y. Yuan, G. Li, F. Zhao, J. Li, Z. Qi, J. Guo, P. Yang, Chem. Eng. J. **515**, 163561 (2025).
[2] L. Wu, F. Zhao, P. Yang, J. Optoelectron. Adv. M. **27**(3-4), 127 (2025).
[3] F. Zhao, Y. Guo, Q. Yang, P. Yang, J. Chu, Optoelectron. Adv. Mat. **19**(3-4), 202 (2025).
[4] F. Zhao, Y. Guo, P. Yang, J. Chu, J. Optoelectron. Adv. M. **27**(5-6), 255 (2025).
[5] F. Zhao, Y. Guo, P. Yang, J. Tao, J. Jiang, J. Chu, J. Alloy. Compd. **930**, 167377 (2023).
[6] H. Yuan, Y. Zhao, J. Duan, B. He, Z. Jiao, Q. Tang, Electrochim. Acta **279**, 84 (2018).
[7] H. Li, G. Tong, T. Chen, H. Zhu, G. Li, Y. Chang, L. Wang, Y. Jiang, J. Mater. Chem. A **6**, 14255 (2018).
[8] P. Teng, X. Han, J. Li, Y. Xu, L. Kang, Y. Wang, Y. Yang, T. Yu, ACS Appl. Mater. Inter. **10**, 9541 (2018).
[9] F. Zhao, J. Zhou, J. Tao, Y. Guo, J. Jiang, J. Chu, J. Alloy. Compd. **897**, 162741 (2022).
[10] Y. Guo, F. Zhao, P. Yang, M. Gao, J. Shen, J. Tao, J. Jiang, J. Chu, J. Mater. Chem. A **11**, 6474 (2023).
[11] S. K. Shil, F. Wang, Z. Lai, Y. Meng, Y. Wang, D. Zhao, M. K. Hossain, K. O. Egbo, Y. Wang, K. M. Yu, J. C. Ho, Nano Res. **14**, 4116 (2021).
[12] J. Li, Y. Lv, H. Han, J. Xu, J. Yao, Materials **15**, 2883 (2022).
[13] A. Hiltunen, N. Lamminen, H. Salonen, M. Liu, P. Vivo, Sustainable Energy & Fuels **6**, 217 (2022).
[14] F. Umar, J. Zhang, Z. Jin, I. Muhammad, X. Yang, H. Deng, K. Jahangeer, Q. Hu, H. Song, J. Tang, Adv. Opt. Mater. **7**, 1801368 (2019).
[15] A. Singh, K. M. Boopathi, A. Mohapatra, Y. F. Chen, G. Li, C. W. Chu, ACS Appl. Mater. Inter. **10**, 2566 (2018).
[16] A. Singh, S. Najman, A. Mohapatra, Y. Lu, C. Hanmandlu, C. Pao, Y. Chen, C. Lai, C. Chu, ACS Appl. Mater. Inter. **12**, 32649 (2020).
[17] M. Ahmed, A. Bakry, A. Qasem, H. Dalir, Opt. Mater. **113**, 110866 (2021).
[18] Y. Zhao, Y. Wang, J. Duan, X. Yang, Q. Tang, J. Mater. Chem. A **7**, 6877 (2019).
[19] H. Guo, Y. Pei, J. Zhang, C. Cai, K. Zhou, Y. Zhu, J. Mater. Chem. C **7**, 11234 (2019).
[20] X. Liu, X. Tan, Z. Liu, H. Ye, B. Sun, T. Shi, Z. Tang, G. Liao, Nano Energy **56**, 184 (2019).
[21] K. M. Mccall, C. C. Stoumpos, S. S. Kostina, M. G. Kanatzidis, B. W. Wessels, Chem. Mater. **29**, 4129 (2017).
[22] B. Dhanabalan, Y. Leng, G. Biffi, M. Lin, P. Tan, I. Infante, L. Manna, M. P. Arciniegas, R. Krahne, ACS Nano **14**, 4689 (2020).

*Corresponding author: fzhaobs@126.com; yxguo@shnu.edu.cn